



**HAL**  
open science

# The transition from ancient to modern-style tectonics: insights from lithosphere dynamics modelling in compressional regimes

Jonathan Poh, Philippe Yamato, Thibault Duretz, Denis Gapais, Patrick  
Ledru

## ► To cite this version:

Jonathan Poh, Philippe Yamato, Thibault Duretz, Denis Gapais, Patrick Ledru. The transition from ancient to modern-style tectonics: insights from lithosphere dynamics modelling in compressional regimes. *Gondwana Research*, 2021, 99, pp.77-92. 10.1016/j.gr.2021.06.016 . insu-03270651

**HAL Id: insu-03270651**

**<https://insu.hal.science/insu-03270651>**

Submitted on 25 Jun 2021

**HAL** is a multi-disciplinary open access archive for the deposit and dissemination of scientific research documents, whether they are published or not. The documents may come from teaching and research institutions in France or abroad, or from public or private research centers.

L'archive ouverte pluridisciplinaire **HAL**, est destinée au dépôt et à la diffusion de documents scientifiques de niveau recherche, publiés ou non, émanant des établissements d'enseignement et de recherche français ou étrangers, des laboratoires publics ou privés.

## Journal Pre-proofs

The transition from ancient to modern-style tectonics: insights from lithosphere dynamics modelling in compressional regimes

Jonathan Poh, Philippe Yamato, Thibault Duretz, Denis Gapais, Patrick Ledru

PII: S1342-937X(21)00189-1  
DOI: <https://doi.org/10.1016/j.gr.2021.06.016>  
Reference: GR 2607

To appear in: *Gondwana Research*

Received Date: 3 September 2020  
Revised Date: 7 June 2021  
Accepted Date: 21 June 2021



Please cite this article as: J. Poh, P. Yamato, T. Duretz, D. Gapais, P. Ledru, The transition from ancient to modern-style tectonics: insights from lithosphere dynamics modelling in compressional regimes, *Gondwana Research* (2021), doi: <https://doi.org/10.1016/j.gr.2021.06.016>

This is a PDF file of an article that has undergone enhancements after acceptance, such as the addition of a cover page and metadata, and formatting for readability, but it is not yet the definitive version of record. This version will undergo additional copyediting, typesetting and review before it is published in its final form, but we are providing this version to give early visibility of the article. Please note that, during the production process, errors may be discovered which could affect the content, and all legal disclaimers that apply to the journal pertain.

© 2021 International Association for Gondwana Research. Published by Elsevier B.V. All rights reserved.

# The transition from ancient to modern-style tectonics: insights from lithosphere dynamics modelling in compressional regimes

Jonathan Poh<sup>a,\*</sup>, Philippe Yamato<sup>a,b</sup>, Thibault Duretz<sup>a</sup>, Denis Gapais<sup>a</sup>, Patrick Ledru<sup>c</sup>

<sup>a</sup>Univ Rennes, CNRS, Géosciences Rennes, UMR 6118, 35000 Rennes, France

<sup>b</sup>Institut Universitaire de France (IUF), France

<sup>c</sup>Université de Lorraine, GeoRessources 2, rue du Doyen Marcel Roubault TSA 70605 54518 Vandoeuvre-lés-Nancy cedex FRANCE

---

## Abstract

Orogens are traditionally classified according to their tectonic style. Paleoproterozoic tectonics is referred to as “ancient-style tectonics” while Proterozoic tectonics is referred to as “modern-style tectonics”. Ancient-style tectonics is characterised by distributed vertical structures and low topography gradients, often associated with diapirism and partial melting. In contrast, modern-style tectonics involve prominent strain localisation and the formation of thrusts, nappes and high topographic gradients. However, the parameters controlling the transition from ancient to modern-style tectonics are poorly understood. To quantify this transition, a combination of 1D and 2D high resolution lithospheric-scale thermo-mechanical models was conducted. The parameters controlling the strength of the lithosphere (i.e., Moho temperature, strain rate, crustal rheology, crustal radiogenic heat production and role of shear heating) were investigated in detail. Our results show that tectonic style is controlled by the maximum of crustal strength (shear stress). Modern-style tectonics is observed to occur when the maximum of crustal strength is greater than 300 MPa. At the opposite, a maximum crustal strength lower than 300 MPa leads to ancient style tectonic structures. Therefore, crustal rheology, temperature and background strain rate significantly influence the transition from ancient to modern-style tectonics. Shear heating remains a key factor in promoting strain localisation in modern-style tectonics. Crustal radiogenic heat production has a moderate influence by increasing/decreasing the tendency for faulting within the crust. This crustal strength criterion also provides an excellent fit for a second potential proxy: a localisation

---

\*Corresponding author

Email address: jonathanpoh87@gmail.com (Jonathan Poh)

1 criterion of ca. 225°C. These two proposed proxies can be used interchangeably to  
2 predict the transition from ancient to modern-style tectonics.

3  
4 *Keywords:* rheology of the lithosphere, shear heating, modern tectonics, ancient  
5 tectonics, strength of the lithosphere, strain localisation  
6  
7

---

## 8 **1. Introduction**

### 9 10 *1.1. Two different tectonic styles across geological times*

11 Tectonic styles on Earth have evolved throughout geological time. Field  
12 observations from Archean and Paleoproterozoic cratons show specific structural  
13 and metamorphic features (e.g., Cagnard et al., 2011; Chardon et al., 2009;  
14 Choukroune et al., 1995; Condie and Benn, 2006; Gapais et al., 2014; Gapais,  
15 2018). Widespread structures observed at the upper parts of the crust present steep  
16 cleavages and plunging stretching lineations, and are associated with low  
17 metamorphic grades up to greenschist facies (see Gapais et al., 2009; Chardon et al.,  
18 2009). The exhumed lower crust is marked by widespread distributed strains with  
19 vertical stretching lineations and is often associated with partially molten supracrustal  
20 rocks reaching, in some places, granulite metamorphic facies conditions (Pressure ( $P$ )  
21  $\leq 1$  GPa, Temperature ( $T$ )  $\leq 850^\circ\text{C}$ , Bouhallier et al., 1995; Cagnard et al., 2006,  
22 2007, 2011; Chardon et al., 2009; Choukroune et al., 1995; Gapais et al., 2005,  
23 2014). One important characteristic is that no major jumps in metamorphic facies  
24 conditions has been observed between the different tectonic units. This is seen from  
25 the retrogression of Archean granulite facies assemblages towards the  
26 Paleoproterozoic amphibolite facies assemblages from most Archean belts and  
27 Paleoproterozoic belts such as the 3.0 Ga Archean East Dharwar Craton (e.g.,  
28 Bouhallier et al., 1995; Chardon et al., 2011, 2009), the 1.69 Ga Terre Adélie Craton in  
29 Antarctica (Gapais et al., 2008), the Thompson Nickel Belt in Canada (Gapais et al.,  
30 2005, 2014), and in the 1.9 Ga Paleoproterozoic Svecofennides (e.g., Cagnard et  
31 al., 2007). Furthermore, it is also argued that the downward and lateral motions in the  
32 upper and lower portions of the crust, respectively, occur in a lithosphere that consists  
33 of a mechanically weak crust and mantle (i.e., *crème brûlée* lithosphere; Burov et al.,  
34 2006; Burov, 2011, and Fig. 1A left), due to the presence of a hot thermal gradient.  
35 Previous numerical studies indicate that these deformation features are caused by

36 plutonism, capable of generating lateral flows perpendicular to the direction of  
37 shortening while being marked with low topography (e.g., Duclaux et al., 2007;  
38 Cruden et al., 2006; Rey and Houseman, 2006). This tectonic style can be classified  
39 as ancient-style tectonics as these deformation features have been observed.

40 In contrast, modern-style tectonics (i.e., Phanerozoic), is characterised by different  
41 structural and metamorphic features (Gapais et al., 2009, and references therein).  
42 Deformation styles are characterised by well-defined rock units separated by major  
43 shear zones. Some rock units now exhumed at the surface, can show in some  
44 places, high pressure metamorphic conditions ( $P \geq 1.0$  GPa,  $T \geq 500^\circ\text{C}$ ). These  
45 exhumed blueschist or eclogite facies rocks are directly related to the development of  
46 major shear zones (i.e., lithospheric-scale thrusts, normal faults and nappe stacks)  
47 associated with the generation of high topography. These modern-style tectonics are  
48 generally linked to colder and mechanically strong lithospheres (jelly sandwich in  
49 Jackson (2002) and Fig. 1A, right) to be able to support topography and  
50 macrostructures (Burov et al., 2006). These structural and metamorphic features are  
51 commonly documented in modern-style orogens as seen in the ca. 50 Ma Himalayas  
52 (e.g., de Sigoyer et al., 2004), in the ca. 35 Ma European Alps (e.g., Schmid et al.,  
53 2017), and in the ca. 5 Ma Taiwan Orogeny (e.g., Yamato et al., 2009).

54 From a geodynamical point of view, the transition from ancient to modern-style  
55 tectonics is associated with the gradual evolution from 'rips and plumes' tectonics  
56 towards modern plate tectonics (e.g., Gerya, 2019a; Palin et al., 2020; Palin and  
57 Santosh, 2020; Brown et al., 2020, and references therein). Several proxies have  
58 been discovered to track the evolution of this transition. The first proxy relates to the  
59 distribution of metamorphic rocks throughout time (e.g., Brown, 2006; Brown and  
60 Johnson, 2018; Holder et al., 2019). A diagnostic feature for modern plate tectonics  
61 is the presence of a paired distribution of metamorphic temperatures and pressures  
62 (Brown, 2006; Miyashiro, 1961). The statistical analysis determined a non-gaussian  
63 distribution from 2.2 – 1.4 Ga, evolving towards a distinctive bimodal distribution in  
64 rock samples after 1.4 Ga (Holder et al., 2019). The analysis also demonstrated a  
65 distinct divergence of low and high metamorphic T/P ratio in metamorphic rocks,  
66 reflecting the secular cooling of the Earth. Additionally, a similar thermal divergence  
67 can be measured in magma temperatures from greenstone belts and komatiites at  
68 2.5 – 2.0 Ga (Condie et al., 2016). Previous geochemistry studies on the Earth's

69 mantle and rocks formed determined that the lithosphere have undergone  
70 irreversible geochemical differentiation (e.g., Anderson, 2002; Martin and Moyen,  
71 2002; Tang et al., 2016; Johnson et al., 2019; Nebel et al., 2018; Capitanio et al.,  
72 2019; Johnson et al., 2019). For instance, the presence or absence of plagioclase  
73 within tonalite–trondhjemite–granodiorite rocks (TTGs) provides a proxy for slab  
74 melting depth and geothermal gradient (Martin and Moyen, 2002). Martin and Moyen  
75 (2002) indicate that the secular cooling of the lithosphere (i.e., a reduction of the  
76 radiogenic heat production produced in crust and heat flow output from the mantle)  
77 increased the melting depth where plagioclase is stable. This secular cooling is also  
78 linked to the changes in crustal chemistry observed in the transition from Archean  
79 granitoid intrusions of TTGs to potassic (K) granite suites (Nebel et al., 2018). The  
80 source for the felsic material originates from these ‘asymmetric drips’ of the melting  
81 lithospheric mantle. Thermo-mechanical models conducted in Nebel et al. (2018) and  
82 Capitanio et al. (2019) indicate that these melts produce hot thermal-depth gradients  
83 (up to  $30^{\circ}\text{C.km}^{-1}$ ) that create a feedback loop of concentrated melting process that  
84 strengthen the lithospheric mantle. The injection of more felsic melts into the mantle  
85 through localised episodes of ‘proto-subduction’ could explain the changes in the  
86 felsic composition of the TTGs, increasing crustal strength (Hawkesworth and Brown,  
87 2018; Johnson et al., 2019; Nebel et al., 2018; Rey et al., 2014; Rey and Coltice,  
88 2008). Additionally, MgO content in igneous and metamorphic rocks marks the  
89 transition of Archean upper crust from highly mafic at 3.0 Ga to felsic at 2.5 Ga (Tang  
90 et al., 2016). Therefore, the secular cooling of the lithosphere is strongly associated  
91 with the critical parameters that control the resultant tectonic style (Lenardic, 2018).

92 Recent field studies in the Paleoproterozoic Lapland Granulite belt and in the  
93 Sveconfennian domain in Finland (Cagnard et al., 2011, and references therein)  
94 provide evidence that the transitional tectonics regime feature consists in a  
95 combination of modern and ancient tectonic modes, according to the nature  
96 (strength) of involved converging plates and associated thermal states (Cagnard et  
97 al., 2011; Lenardic, 2018). Field observations indeed show a widespread of vertical  
98 thrusts formed due to a regional-scale horizontal shortening (i.e., ancient-style  
99 tectonics) associated with metamorphism in sediments that reached  $P > 600$  MPa  
100 and  $T > 750^{\circ}\text{C}$  (Cagnard et al., 2011). The occurrence of high-grade shear zones  
101 (i.e., modern-style structures), which is coeval with widespread partial melting of the

102 sediments at low pressure is also observed. Lastly, retrograde metamorphism  
103 analysis by Cagnard et al. (2011) indicates a protracted exhumation activity (ca. 20 –  
104 30 Myrs) that is interpreted as the result of distributed erosion process (i.e., ancient-  
105 style tectonics). Therefore, the structural and metamorphic evolution observed in the  
106 Lapland Granulite belt suggests that different tectonic styles can coexist. This change  
107 of tectonic style is in contrast to the neighbouring Sveconfennian domain which  
108 presents deformation features in agreement with ancient-style tectonics (Cagnard et  
109 al., 2007; Choukroune et al., 1995) while it is of similar age (1.9 – 1.89 Ga). This  
110 corresponds to the age of the unequivocal oldest subduction-related high pressure  
111 eclogite of 2.1 Ga (see Palin et al., 2020); a potential age of the transition between  
112 modern and ancient-style tectonics. The period of the first occurrence of plate  
113 tectonics evidence remains debatable even though decades-worth of published  
114 studies and several ages ranging from 4.0 Ga Hadean to 1.0 Ga Neoproterozoic are  
115 proposed (Palin et al., 2020; Palin and Santosh, 2020). The latest proposed age for  
116 the first evidence of global plate tectonics is 3.0 Ga as reviewed in Palin and  
117 Santosh (2020). This proposed age corresponds to earlier formations of  
118 supercontinents such as ca. 3.0 Ga Ur and ca. 2.7 – 2.5 Ga Kenorland (Rogers and  
119 Santosh, 2004).

## 120 *1.2. Strength of the lithosphere and parameters to test*

121 Strength of the lithosphere depends on four main parameters that control the  
122 location of coupling/decoupling horizons within the lithosphere and the magnitude of  
123 stresses (Fig. 1A): strain rate, temperature, crustal radiogenic heat production, and  
124 material properties. Using numerical models, it is possible to test a broad range of  
125 strength configurations of the lithosphere to determine what causes the transition from  
126 ancient to modern-style tectonics and to investigate the following questions:

- 127 1. What parameter controls the deformation at the crust and the lithospheric  
128 mantle?
- 129 2. Can a transition from ancient to modern-style tectonics be identified and  
130 quantified?
- 131 3. What controls the occurrence of localised deformation?  
132

133 The general consensus states that the thermal state of the lithosphere dictates the  
134 resultant tectonic style. Numerical models suggest that transitional tectonics occurred

135 at mantle temperature up to 200°C higher than today and was triggered by the  
136 generation of continental crust and the stabilisation of cratons (e.g., Sizova et al.,  
137 2010, 2015; Perchuk et al., 2018). However, a recent thermo-mechanical study  
138 indicated that the shortening rate, which can vary over several orders of magnitude,  
139 also plays an important role (Poh et al., 2020). High shortening rates ( $\dot{\epsilon}_{BG} > 1 \times 10^{-15} \text{ s}^{-1}$ )  
140 favours the formation of asymmetric deformation zones (i.e., modern-style  
141 tectonics) while low shortening rates ( $\dot{\epsilon}_{BG} < 1 \times 10^{-15} \text{ s}^{-1}$ ) favour the development of  
142 distributed deformation zones and vertical structures (i.e., ancient-style tectonics). In  
143 Poh et al. (2020), the study was conducted at a high crustal radiogenic heat  
144 production ( $H_R = 2.0 \mu\text{W}\cdot\text{m}^{-3}$ ) to mimic conditions during the Precambrian. Modern-  
145 style lithospheres however, are considered to have lower crustal radiogenic heat  
146 production values (Condie and Benn, 2006) or to present a localised distribution of  
147 high heat producing rocks (e.g., Faccenda et al., 2008). Furthermore, shear heating  
148 has also been identified as a mechanism of crustal and lithosphere-scale shear  
149 localisation (e.g., Thielmann and Kaus, 2012; Duretz et al., 2014; Kiss et al., 2019;  
150 Auzemery et al. 2020). It is thus important to understand the role of shear heating in  
151 the transition between ancient and modern-style tectonics.

152 In this contribution, a series of 2D numerical models implying a lithosphere  
153 subjected to a compressive regime have been performed to explore a wide range of  
154 parameters: strain rate, Moho temperature, crustal rheology, radiogenic heat  
155 production values. Each of these parameters affect the strength of the crust. In order  
156 to identify the parameters that control the transition between the different tectonic  
157 styles. 3 main factors are particularly studied from our models: (i) the distribution of  
158 the deformation and shear zone generation at the upper parts of the crust but also  
159 within the lithospheric mantle, (ii) the topography evolution and its range of  
160 topography, and (iii) the distribution of the  $P$ - $T$  field. The impact of shear heating on  
161 each tectonic style was also investigated.

## 2. Numerical Approach

### 2.1. Governing equations

Two-dimensional (2D) thermo-mechanical models were used to simulate the shortening of a visco-elasto-plastic continental lithosphere. The 2D finite-difference, marker- in-cell code (MDoodz; Duretz et al., 2016) used in this investigation solves the equations of momentum, mass conservation and heat, which are formulated as:

$$\frac{\partial \tau_{ij}}{\partial x_j} - \frac{\partial P}{\partial x_i} = -\rho^{\text{eff}} g_i \quad (1)$$

$$\frac{\partial v_i}{\partial x_i} = 0, \quad (2)$$

$$\rho^{\text{eff}} C_p^{\text{eff}} \frac{dT}{dt} = \frac{\partial}{\partial x_i} k \frac{\partial T}{\partial x_i} + H_R + H_S + H_L + H_A, \quad (3)$$

where  $\tau_{ij}$  correspond to the deviatoric stress tensor,  $P$  is total pressure,  $v_i$  represents the velocity vector components,  $\rho$  is the density,  $T$  is the temperature,  $C_p$  is the specific heat capacity, and  $k$  is the thermal conductivity. In Eqn. 3, the rocks' effective density ( $\rho^{\text{eff}}$ ) and heat capacity ( $C_p^{\text{eff}}$ ) are only considered when the rock reach partial melting conditions (see Sec. 2.1.2). The heat equation includes the effect of radiogenic heat production ( $H_R$ ), latent heat of production or consumption ( $H_L$ ), adiabatic heat ( $H_A$ ), and shear heating ( $H_S$ ). The subscript indexes  $i$  and  $j$  denote the Einstein notation for spatial directions.

The Boussinesq approximation is applied to the models (in Eqn. 2). This approximation assumes that the impact of volume changes is neglected.

Shear heating ( $H_S$ ) is evaluated by the deviatoric stress and the dissipative part of the strain rate tensor, which is formulated as:

$$H_S = (\dot{\epsilon}_{xx} - \dot{\epsilon}_{xx}^{\text{el}}) \tau_{xx} + (\dot{\epsilon}_{zz} - \dot{\epsilon}_{zz}^{\text{el}}) \tau_{zz} + 2(\dot{\epsilon}_{xz} - \dot{\epsilon}_{xz}^{\text{el}}) \tau_{xz} \quad (4)$$

### 2.1.1. Maxwell visco-elasto-plastic rheology

The lithosphere is considered as a Maxwell visco-elasto-plastic medium, which assumes that viscous, plastic, and elastic deformations occur concurrently for a given value of deviatoric stress ( $\tau_{ij}$ , see also Yamato et al., 2019, for more details). The deviatoric strain rate tensor ( $\dot{\varepsilon}_{ij}$ ) is then formulated as:

$$\dot{\varepsilon}_{ij} = \dot{\varepsilon}_{ij}^{\text{vis}} + \dot{\varepsilon}_{ij}^{\text{el}} + \dot{\varepsilon}_{ij}^{\text{pl}}. \quad (5)$$

The effective creep viscosity ( $\eta^{\text{eff}}$ ) is computed by following a thermally activated power law that represents the dislocation creep deformation mechanism (e.g., Chopra and Paterson, 1984; Hansen and Carter, 1983; Ranalli, 1995, 1997).  $\eta^{\text{eff}}$  is dependent on the second invariant of the creep strain rate tensor,  $\dot{\varepsilon}_{\text{II}}^{\text{vis}}$  and is computed as:

$$\eta^{\text{eff}} = \frac{\tau_{\text{II}}}{2\dot{\varepsilon}_{\text{II}}^{\text{vis}}} = F A^{-\frac{1}{n}} \dot{\varepsilon}_{\text{II}}^{\text{vis}\left(\frac{1}{n}-1\right)} \exp \frac{Q}{nRT} \exp \frac{aM}{n}, \quad (6)$$

where  $n$ ,  $A$ , and  $Q$  are material parameters derived from laboratory experiments (see Table 1),  $F = \frac{2^{(1-n)/n}}{3^{(n-1)/2n}}$  is the dimension coefficient for triaxial experiments,  $\tau_{\text{II}}$  is the second invariant of the deviatoric stress tensor,  $R = 8.314 \text{ J.mol}^{-1}$  is the gas constant,  $T$  is the temperature (in K),  $a$  is a melt-weakening factor, and  $M$  is the melt fraction (e.g., Hirth and Kohlstedt, 2004).

Pressure-dependent plasticity is modelled using a Drucker-Prager yield surface, and the yield stress is formulated as follows:

$$\sigma^{\text{yield}} = C \cos \phi + P \sin \phi \quad (7)$$

where  $\phi$  and  $C$  are the friction angle and cohesion, respectively (see Table 1).

Density ( $\rho$ ) is assumed to be  $P$ - $T$  dependent seen as:

$$\rho = \rho_0^{\text{solid}} (1 - \alpha(T - T_0))(1 + \beta(P - P_0)) \quad (8)$$

where  $\rho_0^{\text{solid}}$  is the reference density,  $\alpha$  is the thermal expansion, and  $\beta$  is the thermal compressibility (see Table 1).  $T_0$  (= 273.15 K),  $P_0$  (=  $10^5$  Pa), and  $\rho_0$  correspond to reference temperature, pressure, and density, respectively.

### 2.1.2. Partial melting

218 Latent heat ( $H_L$ ) becomes important when partial melting or crystallisation occurs.  
 219 In the case of melting,  $H_L$  operates as a heat sink ( $H_L < 0$ ), while crystallisation  
 220 induces a heat source ( $H_L > 0$ ). When using a single-phase formulation, the effects  
 221 of partial melting can be approximated by: (i) reduction in density with increasing melt  
 222 fraction (ii) lowering the effective viscosity (see Eqn. 6), and (iii) thermal effects due  
 223 to melting and crystallisation processes. The volumetric fraction of melt is assumed to  
 224 increase linearly with temperature, according to these relationships (Burg and Gerya,  
 225 2005; Gerya and Yuen, 2003):

$$226 \quad M = 0, \text{ at } T \leq T_{\text{solidus}}, \quad (9)$$

$$M = \frac{T - T_{\text{solidus}}}{T_{\text{liquidus}} - T_{\text{solidus}}}, \text{ at } T_{\text{solidus}} < T < T_{\text{liquidus}} \quad (10)$$

$$M = 1, \text{ at } T \geq T_{\text{liquidus}} \quad (11)$$

227 where  $T_{\text{solidus}}$  and  $T_{\text{liquidus}}$  are the wet solidus and dry liquidus temperatures of the  
 228 considered rock, respectively (see Table 1 for equations). The volumetric fraction of  
 229 melt ( $M$ ) influences the effective density ( $\rho^{\text{eff}}$ ) of the partially molten rocks as follows:

$$230 \quad \rho^{\text{eff}} = \rho \left( 1 - M + M \frac{\rho_0^{\text{molten}}}{\rho_0^{\text{solid}}} \right) \quad (12)$$

231 where  $\rho_0^{\text{solid}} = \rho_0$  and  $\rho_0^{\text{molten}}$  are liquid densities (see Table 1).

233 Other processes associated with partial melting, such as solid-melt segregation  
 234 and melt extraction, are neglected. This assumption is discussed further in Section  
 235 4.4. The effect of latent heating due to equilibrium melting or crystallisation is included  
 236 implicitly by increasing the effective heat capacity ( $C_p^{\text{eff}}$ ) and the thermal expansion ( $\alpha^{\text{eff}}$ )  
 237 of the partially crystallised molten rocks ( $0 < M < 1$ ) following Burg and Gerya  
 238 (2005).  $Q_L$  is the latent heat of melting of the considered rocks.

239

240

$$C_p^{eff} = C_p + Q_L \left( \frac{\partial M}{\partial T} \right)_P \quad (13)$$

$$\alpha^{eff} = \alpha + \rho \frac{Q_L}{T} \left( \frac{\partial M}{\partial P} \right)_T \quad (14)$$

241 Advection of composition, temperature, strain, and stress fields is carried out in a  
 242 Lagrangian manner using the particle-in-cell method. Particles are advected at each  
 243 time step in an explicit manner using a 1<sup>st</sup> order in time and 4<sup>th</sup> order in space Runge-  
 244 Kutta scheme. The Courant condition ratio is set at 0.3 for all 2D numerical models.

## 245 2.2. Model setup

246 The numerical model consists of 800 (horizontal) by 330 (vertical) uniformly  
 247 distributed nodes, which gives the physical dimensions of 400 km by 165 km for the  
 248 model box and results in a grid spacing of 500 m (Fig. 1B). The top of the model is a  
 249 free surface (Duretz et al., 2016). The geological model consists of a rectangular 30  
 250 km thick crust that is subdivided into two homogeneous components: a 2.5 km  
 251 sedimentary layer over a 27.5 km granitic crust. This value is chosen as an average  
 252 crustal thickness. The initial thickness of the crust is then free to thicken during the  
 253 simulation, subjected to boundary conditions and the material properties used. This  
 254 study is thus restricted to the case of a homogeneous visco-elasto-plastic crust. A  
 255 circular sedimentary inclusion (weak seed) with a diameter of 2 km was placed at a  
 256 depth of 8.5 km and at  $x = -10$  km to initiate the deformation. Rheological laws used  
 257 in the models and their thermal parameters are presented in Table 1.

258 To simulate a compressive regime, a fixed velocity ( $v$ ) corresponding to an  
 259 average strain rate ( $\dot{\epsilon}_{BG}$ ) normal to the lateral boundaries is imposed. Material inflow  
 260 is compensated by imposing a normal outflow at the bottom boundary ( $v_{bottom}$ ), thus  
 261 satisfying the mass conservation in the whole model domain. Since the size of the  
 262 model and applied shortening velocity remains constant throughout the simulation,  
 263 the corresponding average strain rate (i.e.,  $\dot{\epsilon}_{BG}$ ) applied at the boundaries is also  
 264 constant. The 2D parametric study is conducted over a wide range of initial  
 265 geotherms ( $T_{Moho} = 850^\circ\text{C}$  to  $550^\circ\text{C}$ ) and shortening rates ( $\dot{\epsilon}_{BG} = 1 \times 10^{-14} \text{ s}^{-1}$  to  $2 \times 10^{-16} \text{ s}^{-1}$ ) to cover a wide range of lithospheric strength configurations. The initial

267 geotherm was computed using thermal parameters (presented in Table 1) and a fixed  
 268 temperature boundary of 1330°C at the base of an adiabatic asthenosphere. The  
 269 temperature field was obtained by solving the heat equation until steady state and  
 270 by varying the thickness of the lithosphere until the desired Moho temperature was  
 271 reached. This constrains the initial thickness of the lithosphere.

272 Fig. 1A shows the yield strength envelopes and geotherms corresponding to the  
 273 end-member tectonic models at initial conditions. These models were obtained by  
 274 considering a combination of temperature field and strain rate ( $T_{\text{Moho}}$  and  $\dot{\epsilon}_{\text{BG}}$  values  
 275 from left to right in Fig. 1A: [750°C,  $1.0 \times 10^{-15} \text{ s}^{-1}$ ], [550°C,  $1.0 \times 10^{-14} \text{ s}^{-1}$ ]).

276

### 277 3. Results

278

279 For the initial 2D parametric study of 16 numerical simulations, two governing  
 280 parameters are considered: shortening rates ( $\dot{\epsilon}_{\text{BG}}$ ) and Moho temperature ( $T_{\text{Moho}}$ ).  
 281 The summary of these experiments are shown in Fig. 2 and Supplementary Data,  
 282 Fig. S1. Two main deformation styles can be characterised. They can be presented  
 283 using two models and represent the ancient and modern-style tectonics;  
 284 corresponding to the parameters marked as by red and blue squares (in Figs. 2, 3  
 285 and 4).

#### 286 3.1. End-member tectonic styles and reference models

287 The reference model that generated ancient-style tectonics has an initial Moho  
 288 temperature of 750°C and a background strain rate of  $1 \times 10^{-15} \text{ s}^{-1}$  (Fig. 3A). After ca.  
 289 320 km of horizontal shortening, the Moho remained flat. In the upper portions of the  
 290 crust, localised strain area within sedimentary cusps are vertically oriented.  
 291 Additionally, regions of high viscosity beneath the sedimentary cusps at 25 km depth  
 292 are formed and facilitate strain localisation ( $\eta_{\text{eff}} > 10^{22} \text{ Pa.s}$  in  $x = -75 \text{ km}$  and  $+45 \text{ km}$   
 293 in Fig. 3A). The evolution of topography depicts two deformation stages (buckling  
 294 and cusping) expressed as a periodic sequence of crests and troughs (Fig. 4A). The  
 295 maximum topographic range (i.e., the difference between the maximum and the  
 296 minimum of topography) is 2.0 km (Fig. 4A) and is in agreement with the values  
 297 expected until Neoproterozoic (Rey and Coltice, 2008). Additionally, horizontal isotherms  
 298 and isobars indicates an absence of major reverse metamorphic pressure breaks.  
 299 When compared to the rest of the parametric study, this trend of distributed  
 300 deformation at the upper parts of the crust and minimal strain localisation of the

301 lithospheric mantle (i.e., flat Moho) continues in models with high Moho temperatures  
 302 ( $T_{\text{Moho}} \geq 650^\circ\text{C}$ ). A  $+100^\circ\text{C}$  increase to  $T_{\text{Moho}} = 850^\circ\text{C}$  leads to the formation of well-  
 303 established crustal convection in the lower parts of the crust. The lateral thickness of  
 304 the buried sediments has decreased and the formation of sedimentary cusps begins.  
 305 Rapid crustal convection with limited burial of the sedimentary layer occurs when  
 306 strain rate is decreased by an order of magnitude ( $\dot{\epsilon}_{\text{BG}} = 2.0 \times 10^{-16} \text{ s}^{-1}$ ). An order of  
 307 magnitude increase in strain rate ( $\dot{\epsilon}_{\text{BG}} = 1.0 \times 10^{-14} \text{ s}^{-1}$ ) leads to the generation of  
 308 undeformed zones marked by high viscosity triangular wedges ( $\eta \geq 10^{23} \text{ Pa}\cdot\text{s}$ ) in the  
 309 upper parts of the crust and increases strain localisation in the lithospheric mantle  
 310 (i.e., from flat Moho to slightly uneven Moho).

311 The reference model for modern-style tectonics corresponds to an initial Moho  
 312 temperature of  $550^\circ\text{C}$  and a background strain rate of  $1 \times 10^{-14} \text{ s}^{-1}$  (Fig. 3B). After ca.  
 313 320 km of horizontal shortening, the lithospheric mantle shows asymmetric burial of  
 314 the Moho reaching ca. 100 km depth. This burial depth reached by the lithospheric  
 315 mantle indicates that subduction initiated. The upper part of the crust is affected by  
 316 multiple thrusts (Fig. 3B). Accumulated strain maps indicate the formation of shear  
 317 zones within both the crust and the lithospheric mantle. The evolution of the  
 318 topography shows a three-stage deformation evolution: (i) Initial buckling of the  
 319 lithospheric mantle that corresponds to the first topographic high occurring during the  
 320 first 60 km of horizontal shortening; (ii) shearing of the lithospheric mantle associated  
 321 to a decrease of the topography; (iii) thrusting of the mantle and the upper parts of  
 322 the crust and formation of periodic topographic crests and troughs with a wavelength  
 323 of 50 km after 240 km of horizontal shortening (Fig. 4B). The maximum topographic  
 324 range achieved in this model after 80% of horizontal shortening is 13.4 km. When  
 325 compared to the rest of the parametric study, similar deformation style persists in  
 326 models with low Moho temperatures ( $T_{\text{Moho}} = 550^\circ\text{C}$ ) for most of the strain-rates and  
 327 one at  $T_{\text{Moho}} = 650^\circ\text{C}$  and  $\dot{\epsilon}_{\text{BG}} = 1.0 \times 10^{-14}$ . When  $T_{\text{Moho}}$  increases, deformation of the  
 328 lithospheric mantle decrease and lithospheric-scale shear zones and uneven Moho  
 329 are progressively replaced by a flat Moho. However, the occurrence of undeformed  
 330 zones marked by high viscosity triangular wedges (i.e., Pop-downs;  $\eta \geq 10^{23} \text{ Pa}\cdot\text{s}$ ) at  
 331 the upper parts of the crust still persist. The amount of deformation at the upper parts  
 332 of the crust decreased with reduced strain rate, concurring with observations in the  
 333 discussion of the ancient-style tectonics reference model.

334 The 2D parametric study confirms that the magnitude of the strain rate controls the  
335 type of crustal deformation feature as shown by Poh et al. (2020). The cusping of the  
336 buried sedimentary rocks occurs at low strain rates ( $\dot{\epsilon}_{BG} \leq 1 \times 10^{-15} \text{ s}^{-1}$ ), whereas  
337 thrusts of the upper parts of the crust is favoured at high strain rates ( $\dot{\epsilon}_{BG} \geq 2 \times 10^{-15} \text{ s}^{-1}$ ).  
338 The intensity of deformation of the lithospheric mantle is suggested to be  
339 significantly controlled by Moho temperatures instead of strain rates. These reference  
340 models are then subjected to further tests (i.e., crustal rheology, crustal radiogenic  
341 heat production, and the role of shear heating).

### 342 3.2. *Effect of shear heating*

343 Figs. 5 and 6 present the two reference models with and without the activation of  
344 shear heating, respectively. The ancient-style reference model remains similar despite  
345 neglecting shear heating (Fig. 5B). The upper parts of the crust displayed similar  
346 distributed cusping of the sedimentary layer and homogeneous thickening of the crust  
347 with a flat Moho. The thickened crust presents a thick lower parts of the crust bounded  
348 by the 700°C isotherm.

349 The effects of shear heating are more important for the modern-style tectonics  
350 model (Fig. 6B). Indeed, in mechanically strong lithospheres, conditions for strain  
351 localisation by shear heating are easily met (Fig. 1B). Shear zone formation within  
352 the lithospheric mantle leads to a decrease of the viscosity (from  $\eta_{\text{eff}} = 10^{23} \text{ Pa}\cdot\text{s}$  to  
353  $10^{21} \text{ Pa}\cdot\text{s}$ ). The upper part of the crust also exhibits prominent thrusts ( $x = +150 \text{ km}$  in  
354 Fig. 6A, top). When shear heating is neglected, strain localisation does not occur  
355 within the lithospheric mantle (i.e., subduction initiation fails, Fig. 6B). The upper parts  
356 of the crust exhibits buckling with the generation of overpressured area ( $> 500 \text{ MPa}$   
357 at ca. 15 km depth). The brittle domains of both the crust and mantle show numerous  
358 frictional-plastic shear bands.

### 359 3.3. *Effect of crustal rheology*

360 In addition to the variation of shortening rate and geotherms, crustal strength is  
361 also controlled by the composition of the lithosphere (Fig. 1A). The crustal rheology  
362 dictates the depth of the brittle-ductile transition (e.g., Fig. 1A left and right), which  
363 subsequently affects the resulting deformation (e.g., Yamato et al., 2008; Duretz and  
364 Gerya, 2013a; Liao and Gerya, 2017). The crustal rheology applied to the 2D  
365 parametric study (Fig. 3 and Supplementary Data, Fig. S1) is Dry Westerly Granite

366 (Hansen and Carter, 1983). The role of the rheology is tested by varying the crustal  
367 lithology and its associated flow law parameters (i.e., Dry Quartzite (Ranalli, 1995,  
368 1997) and Dry Felsic Granulite (Ranalli, 1995)) on the two reference models (Figs. 7  
369 and 8). Models with a weaker crust (i.e., using Dry Quartzite) are shown in Figs. 7A  
370 and 7B; whereas the models with a stronger crust (i.e., using dry felsic granulite) are  
371 presented in Figs. 8A and 8B.

372 For the ancient-style tectonic model (Fig. 7A), the presence of a weak crust leads  
373 to a distributed crustal deformation. Burial of the sedimentary layer by cusping is less  
374 pronounced ( $< 10$  km depth) compared to the reference model in which the cusps  
375 reached ca. 15 km depth for a similar amount of shortening (Fig. 3A). Most tectonic  
376 structures in the buried sediments remain oriented vertically as in the reference model.  
377 However, strain is more distributed. Convection of the partially molten parts of the  
378 lower parts of the crust is observed as in the reference model. The topographic range  
379 reduces from 2.0 km to 1.4 km. When applying a weak crustal rheology to the  
380 modern-style tectonic model, Pop-downs at the upper parts of the crust are formed.  
381 The sedimentary layer is buried periodically (Fig. 7B). The lithospheric mantle  
382 experienced a downward deflection reaching 100 km depth which is accompanied by  
383 the thickening of the crust at ca. 100 km depth in the middle. The topographic range  
384 increased (from 13.4 km to 15.4 km) due to the decoupling of the upper parts of the  
385 crust and the lithospheric mantle (strain is localised here instead).

386 The use of a felsic granulite rheology generated changes in deformation patterns  
387 for both tectonic models (Fig. 8A and B). In Fig. 8A, the ancient-style tectonic model  
388 with a stronger crust depicts the appearance of reverse faults in the upper parts of  
389 the crust while maintaining an undeformed lithospheric mantle. Although cusping of  
390 sediments still occurs, the generation of dipping faults suggests a transition from a  
391 distributed deformation to a localised and asymmetric deformation. Crustal convection  
392 is not present at the lower part of the crust. The topographic range has increased  
393 from 2.0 km to 4.5 km. Applying a stronger crust to the modern-style tectonic model  
394 generates deformation features similar to the modern-style tectonics reference model  
395 (in Fig. 3B and 8B). Thrusts occurs in both upper parts of the crust and lithospheric  
396 mantle. The only difference is the presence of an upward deflection of the lithospheric  
397 mantle (Fig. 8B), which greatly increases topographic range (from 13.4 km to ca.  
398 18.1 km). Therefore, the effect of introducing stronger crustal rheology leads to the

399 formation of modern-style deformation features in the model (i.e., faults and thrusts at  
400 the upper parts of the crust and strain localisation at the lithospheric mantle).

#### 401 3.4. Effect of crustal radiogenic heat production ( $H_R$ )

402 The value of  $H_R$  used for the crust and sedimentary layer in all the above-  
403 described models was kept constant ( $2.0 \mu\text{W.m}^{-3}$ ). To address the large range of  
404 possible  $H_R$  values from previous compilations (e.g., up to  $4.2 \mu\text{W.m}^{-3}$  in Mareschal  
405 and Jaupart, 2013; Jaupart et al., 2016; Goes et al., 2020), the median value was  
406 selected. Two additional values were also tested (Moderate  $H_R = 1.3 \mu\text{W.m}^{-3}$  and low  
407  $H_R = 0.6 \mu\text{W.m}^{-3}$ ). These values are also in agreement with previous compilations  
408 from Archean TTG granites (Bea, 2012; Rolandone et al., 2002). Initial thickness of  
409 the lithospheric mantle is reduced when applying a lower crustal  $H_R$  to the model,  
410 while evaluating the Moho temperature using the thermal equation (in Section 2.2).  
411 This corresponds to lithospheric thickness of 77 km and 66 km for the ancient-styled  
412 at moderate  $H_R$  and low  $H_R$ , respectively. Additionally, the initial thickness of the  
413 lithosphere for modern-styled reference models is 143 km and 103 km at moderate  
414 and low  $H_R$  values. Results and the adjusted initial thickness of the lithospheric  
415 mantle are presented in Figs. 9 and 10.

416 At moderate and low  $H_R$  values for the ancient-style reference model (Fig. 9A and  
417 B), the deformation style remains similar. Cusping of the sedimentary layer allows  
418 sediments to reach burial depths of ca. 25 km depth. Strain is localised within  
419 vertically buried sediments. Both moderate and low  $H_R$  model variants resulted  
420 in a flat Moho, witnessing the absence of strain localization in the mantle  
421 lithosphere. The maximum crustal strength value and the corresponding depth  
422 (i.e., the depth of the brittle-ductile transition) increased from 116 MPa at 8 km  
423 depth (i.e., reference model) to 129 MPa at 9 km depth and 143 MPa at 10 km  
424 depth for moderate and low  $H_R$  model variants, respectively. Additionally, the  
425 maximum strength for the lithospheric mantle has decreased from 172 MPa (in  
426 reference model) to 152 MPa and 136 MPa for the moderate and low  $H_R$  model  
427 variants while maintaining a 30 km brittle-ductile transition depth, respectively.  
428 One major difference is the pressure and temperature of the buried sediments. The  
429 maximum temperature of the sediments in moderate and low  $H_R$  are lower (ca.  
430  $325^\circ\text{C}$  in Fig. 9A and ca.  $400^\circ\text{C}$  in Fig. 9B) than in the reference model at high  $H_R$

431 values (ca. 425°C in Fig. 3A). Although the sediments undergo cusping in both low  
432 and high  $H_R$  values, the sediments in the low  $H_R$  model experiences higher pressure  
433 conditions (ca. 800 MPa) than the sediments at high  $H_R$  value (ca. 500 MPa in Fig.  
434 3A).

435 Applying a lower  $H_R$  for the modern-style tectonics model increases the maximum  
436 crustal strength and depth of the brittle-ductile transition zone of the crust, from 170  
437 MPa at 12 km depth (i.e., reference model) to 184 MPa at 13 km depth (i.e., moderate  
438  $H_R$ ) and 212 MPa at 15 km depth (i.e., low  $H_R$ ) at initial conditions. Applying a  
439 reduced  $H_R$  has a greater effect on the depth and maximum strength of the lithospheric  
440 mantle at initial conditions, from 1093 MPa at 73 km depth (i.e., reference model) to  
441 782 MPa at 53 km depth (i.e., moderate  $H_R$ ) and 663 MPa at 45 km depth (i.e., low  
442  $H_R$ ). However, overall deformation features of the moderate and low  $H_R$  model  
443 variants remained similar (Fig. 10A and B). The crust continues to exhibit  
444 multiple thrusts and major strain localisation occurs within the lithospheric mantle.  
445 For reduced  $H_R$ , faults with dip orientations of 30–35° penetrated deeper within the  
446 crust, increasing the amount of asymmetric deformation. The reduction of  $H_R$  would  
447 therefore accentuate modern-style tectonic behaviours.

### 448 3.5. *The transition from ancient to modern-style tectonics*

449 The two deformation styles characterised in this study complement the results  
450 already obtained in a recent thermo-mechanical study (Poh et al., 2020). The  
451 occurrences of pop-downs and thrusts at the upper parts of the crust are obtained in  
452 models at high strain rates ( $\dot{\epsilon}_{BG} \geq 2 \times 10^{-15}$ ) while sedimentary cusping occurs at low  
453 strain rates ( $\dot{\epsilon}_{BG} \leq 1 \times 10^{-15}$ ). Furthermore, the occurrence of these deformation styles  
454 in wider models can be upscaled. According to Poh et al. (2020), their tectonic  
455 features are comparable to those found in large accretionary terranes (> 400 km) as  
456 seen in Precambrian localities (e.g., the 3.4–2.7 Ga Dharwar Craton in India  
457 (Chardon et al., 2011) and the 1.69 Ga Terre Adélie Craton in Antarctica (Gapais et al.,  
458 2008)).

459 Our 2D parametric study allows the deciphering of two end-member tectonic  
460 models corresponding to the main features of ancient and modern-style tectonics  
461 (Fig. 2). To investigate what controls this transition, we propose a complementary 1D  
462 thermo-mechanical parametric study (Fig. 9A). Fig. 9A shows the strength (shear

463 stress) of the lithosphere computed using Eqns. 6 and 8 for a wide range of Moho  
 464 temperature values ( $T_{\text{Moho}}$  from 525°C to 875°C) and background strain rate values (  
 465  $\dot{\epsilon}_{\text{BG}}$  from  $5 \times 10^{-17} \text{ s}^{-1}$  to  $1 \times 10^{-14} \text{ s}^{-1}$ ). The initial thickness of the lithosphere  
 466 corresponds to the lower part of the model where  $T < 1330^\circ\text{C}$  and the geotherm is  
 467 computed assuming thermal equilibrium.

468 The maximum crustal strength (i.e., the shear stress of the crust at the brittle-  
 469 ductile transition, see Fig. 1A) provides an ideal proxy in explaining the transition  
 470 between tectonic styles. As such, we consider the occurrence of thrusts in the crust  
 471 and presence of the deformed lithospheric mantle as the transition from ancient to  
 472 modern-style tectonics (Fig. 2 and Supplementary Data, Fig. S1). In Fig. 4, this  
 473 transition begins at  $T_{\text{Moho}} = 650^\circ\text{C}$ ,  $\dot{\epsilon}_{\text{BG}} = 1 \times 10^{-14} \text{ s}^{-1}$ ,  $T_{\text{Moho}} = 550^\circ\text{C}$ ,  $\dot{\epsilon}_{\text{BG}} = 2 \times 10^{-15} \text{ s}^{-1}$   
 474 to  $T_{\text{Moho}} = 550^\circ\text{C}$ ,  $\dot{\epsilon}_{\text{BG}} = 1 \times 10^{-15} \text{ s}^{-1}$ . When compared to the 1D parametric study, this  
 475 transition line would correspond to a value of ca. 300 MPa for the crustal strength at  
 476 the brittle-ductile transition. This result shows that any lithosphere with a maximum  
 477 crustal strength less than ca. 300 MPa would lead to ancient-style tectonic features.  
 478 At the opposite, modern-style tectonics will occur for a lithosphere presenting a  
 479 maximum crustal strength higher than 300 MPa (bottom right corner of Fig. 11A).

480 Fig. 11B and 11C display similar results using a different crustal rheology and  
 481 crustal radiogenic heat production, respectively. The shifting of the transition line was  
 482 monitored from the 1D study when changing the rheology of the crust (Fig. 11B) and  
 483 crustal radiogenic heat production (Fig. 11C). An increase in crustal strength expands  
 484 the domain of modern-style tectonics (i.e., transition line moves upwards). Imposing  
 485 a stronger crustal rheology enabled faulting within the crust in Fig. 8A, indicating that  
 486 this transition between ancient to modern-style tectonics exists. At the opposite, a  
 487 decrease in crustal strength increases the domain for ancient-style tectonics.  
 488 Therefore, this numerical study determines that a transition between the two tectonic  
 489 styles exists and can be tracked using crustal strength. A decrease in crustal heat  
 490 production increases crustal strength and thus, expands the domain of modern-style  
 491 tectonics (Fig. 11C). This indicates that reducing crustal  $H_R$  accentuate the generation  
 492 of deformation features akin to modern-style tectonics.

## 493 4. Discussion

494

### 495 4.1. Role of crustal radiogenic heat production ( $H_R$ )

496 The accumulation of sediments during shortening to the concentration of minerals (e.g.,  
497 zircons and monazites) that are enriched in radiogenic heat producing elements (up  
498 to  $5 \mu\text{W}\cdot\text{m}^{-3}$  in Faccenda et al., 2008). Previous thermo-mechanical numerical studies  
499 indicate that the concentration and subsequent burial of such high heat producing  
500 rocks is capable of generating localised thermal anomalies within the lithosphere  
501 (e.g., Faccenda et al., 2008; Gray and Pysklywec, 2010). These thermal anomalies  
502 can lead to the generation of low viscosity regions, that decouple the lower and upper  
503 portions of the crust during orogenesis (Sokoutis and Willingshofer, 2011), and trigger  
504 additional tectonic processes, such as gravitational instabilities (Gerya et al., 2004)  
505 and exhumation (Faccenda et al., 2008).

506 The  $H_R$  value of  $5.0 \mu\text{W}\cdot\text{m}^{-3}$  used in Faccenda et al. (2008) conforms to the upper  
507 limits of  $H_R$  values for Archean TTGs (Bea, 2012) and is considerably higher than our  
508 tested values ( $H_R = 0.6, 1.3$  and  $2.0 \mu\text{W}\cdot\text{m}^{-3}$ ). If we assign such high values to our  
509 reference models, we expect the transition line presented in Fig. 11C to shift  
510 downwards, expanding the domain for ancient-style tectonics. When applied, the  
511 maximum crustal strength for the high  $H_R$  variants of the ancient and modern-style  
512 reference models was at ca. 170 MPa and 310 MPa after 20% of horizontal  
513 shortening, respectively. Using our maximum crustal strength criterion, we predict  
514 that the lithosphere in this modern-style tectonics model will begin to produce some  
515 ancient-style deformation features such as the occurrence either more distributed  
516 deformation at the upper parts of the crust, reduced strain localisation at the  
517 lithospheric mantle, smoother  $P$ - $T$  gradients or lower topographic range.

#### 518 4.2. Importance of shear heating

519 Shear heating has been identified as a natural process to localise and stabilise  
520 deformation at crustal scale (Burg and Schmalholz, 2008). It could be also responsible  
521 for generating inverted metamorphism sequences as observed at the base of tectonic  
522 nappes (Duprat-Oualid et al., 2013). Our models show that shear heating is a key  
523 ingredient that trigger the formation of modern-style tectonic features. Switching off  
524 shear heating causes the lithospheric mantle to buckle and fold (Fig. 6B).

525 However, the role of shear heating for ancient-style tectonics appears to be minor.  
526 It suggests that thermo-mechanical conditions of ancient orogens was not favourable  
527 to strain localisation by shear heating. We consider the development of prominent  
528 shear zones in the mantle as a proxy for subduction initiation; a key ingredient of  
529 modern-style tectonics. We have computed the localisation criterion from Kiss et al.  
530 (2019) to predict the occurrence of subduction initiation via shear heating (i.e.,  $T_{SH}$   
531 value from Kiss et al., 2020). Using the parameters for dislocation creep of dry olivine  
532 (i.e., the lithospheric mantle in our models), the applied velocity difference, the model  
533 length and 200 km of shortening, the criterion is evaluated to be  $T_{SH} - T_{\text{Moho}} > 225^{\circ}\text{C}$   
534 . The results are presented in Fig. 11D. When compared to the models from the 2D  
535 parametric study (in Fig. 3, Supplementary Data, Fig. S1), the area below the  
536 contour of the localisation criteria of  $225^{\circ}\text{C}$  covers the same models that are  
537 identified to generate modern-style tectonics. This is an excellent agreement  
538 between our proposed crustal shear stress criterion (i.e., ca. 300 MPa) and the  
539 prediction of Kiss et al. (2020). Therefore, both criteria can be used to predict the  
540 transition between ancient and modern-style tectonics.

#### 541 4.3. Implications for Plate tectonics

542 Tectonic plates move in part due to the convective process in the mantle. Plates  
543 eventually collide, generating deformation belts characterised by either ancient or modern-  
544 style tectonics. In our study, we associate the onset of thrusts and the generation of  
545 lithospheric-scale shear zones in the lithospheric mantle as indicators for the occurrence  
546 of modern-style tectonics. We observe that crustal faults become prominent when  
547 maximum crustal strength exceeds ca. 300 MPa (e.g., Fig. 8A). In contrast, the  
548 occurrence of periodic formation of pop-downs and an absence of prominent thrusts in  
549 the upper parts of the crust (ancient-like deformation) together with the deformed Moho  
550 (modern-like deformation) indicate that a transitional style can exist. This occurs with  
551 maximum crustal shear stress of ca. 300 MPa (in Fig. 7B). Previous field studies indeed  
552 indicate that both ancient and modern tectonics have occurred coevally as seen in the  
553 review of the Finnish Lapland Granulite belt and the Svecofennian domain (Cagnard et  
554 al., 2007, 2011, and references therein). Our models predict that deformation features  
555 associated with modern-style tectonics will appear when the crust reaches a maximum  
556 shear stress of 300 MPa or a localisation criterion of  $225^{\circ}\text{C}$ , and fulfil the necessary

557 conditions for plate tectonics to occur (e.g., Cawood et al., 2012, 2018).

558

#### 559 *4.4. Limitations of model*

560 In this study, we only used one material to model a homogenous crust (i.e.,  
561 Westerly granite dislocation creep flow law; Hansen and Carter, 1983). The important  
562 point is that crust is modelled by a material with a brittle-ductile transition allowing to  
563 test the influence of changing its rheological structure. While testing different  
564 temperature gradients, strain rates and flow laws, we consider this modelling choice as  
565 representative of the crust. By testing a wide range of the afore-mentioned  
566 parameters, we investigated a large range of possible rheological structures for the  
567 crust. Using other rheological flow laws (see Section 3.3) leads to the same  
568 conclusions concerning the maximum crustal shear stress, allowing to explain the  
569 transition between ancient and modern style tectonics. However, results have to be  
570 taken with caution as they do not consider a crust composed by more layers. Indeed,  
571 rheological layering can have an impact on the structure of orogens (e.g., vergence  
572 of wedges; Vogt and Gerya, 2014), and the convergence margins (e.g. due to  
573 coupling/decoupling processes; Yamato et al., 2008; Duretz and Gerya, 2013b). In  
574 addition, the presence of crustal heterogeneities was not considered. The latter may  
575 induce material instabilities such as folding or necking (e.g., Schmalholz and  
576 Mancktelow, 2016), formation of second order tectonic nappes, or stress and  
577 pressure variations that may affect metamorphism (e.g., Reuber et al., 2016).  
578 Heterogeneities can further reduce the magnitude of stress required for subduction  
579 initiation and may further increase the asymmetry of orogenic wedges, as already  
580 shown in extensional setting (e.g., Petri et al., 2019).

581 Introducing heterogeneities within the crust due to melt extraction process may  
582 also be important. In our model, changes in viscosity, density and latent heat due to  
583 partial melting are implemented (see Section 2.1.2). They therefore account for the first  
584 order effect due to partial melting even though melt extraction is neglected. The effect  
585 of melting in modern-style tectonic models appears minimal but becomes obvious in  
586 ancient style tectonics models where this process leads to crustal convection. In these  
587 models, the percentage of melt within the lower crust is probably overestimated due to  
588 the lack of melt extraction. Consequently, convection in the lower crust is potentially  
589 exaggerated. Two phases flow numerical models (e.g., Keller et al., 2013) could be

590 used in future studies to address this effect in more detail. However, it is important to  
591 note that this method also has limitations as they still struggle to capture end-members  
592 (i.e., 100% solid and to 100% liquid).

593

## 594 **5. Conclusions**

595 A combination of 1D and 2D high-resolution thermo-mechanical numerical models  
596 was used to identify and quantify the transition from ancient to modern-style tectonics.  
597 Four parameters that control the strength of the lithosphere (i.e., strain rate, Moho  
598 temperature, crustal rheology and crustal radiogenic heat production) and the  
599 influence of shear heating were investigated. Strain rate remains a key factor that  
600 dictates tectonic style. Shear heating was found to be essential in modern-style  
601 tectonic models for generating, localising and stabilising strain localisation within the  
602 crust and lithospheric mantle. Crustal radiogenic heat production plays a moderate  
603 role in the transition from ancient to modern-style tectonics. The transitional tectonic  
604 style, which combines features from both ancient and modern-style tectonic models,  
605 was also modelled. Our results suggest that the transition between ancient-style and  
606 modern-style tectonics correspond to a maximum crustal strength at ca. 300 MPa.  
607 Moreover, this crustal strength criterion is in excellent agreement with the localisation  
608 criterion of ca. 225°C found by Kiss et al. (2020), allowing the prediction for shear  
609 zones development in lithospheric-scale models. Therefore, these proxies can be  
610 used interchangeably to predict the transition between tectonic styles.

611

## 612 **Acknowledgements**

613

614 This contribution represents the second part of the first author's PhD thesis and was  
615 supported financially by Orano Mining. The 2D thermo-mechanical code, MDoodz,  
616 can be made available by P. Yamato and T. Duretz upon request. The authors would  
617 like to thank R. Chemillac and C. Cutts of Orano for their feedback to the manuscript.  
618 We would also like to thank T. Gerya for the editorial handling and two anonymous  
619 reviewers for their detailed and constructive reviews.

621

622 **References**

623

624 Anderson, D.L., 2002. The Case for Irreversible Chemical Stratification of the Mantle.

625 Int. Geol. Rev. 44, 97–116. doi:10.2747/0020-6814.44.2.97.

626

627 Auzemery, A., Willingshofer, E., Yamato, P., Duretz, T., Sokoutis, D., 2020. Strain

628 localization mechanisms for subduction initiation at passive margins. Glob. Planet.

629 Change 195, 103323. doi:10.1016/j.gloplacha.2020.103323.

630

631 Bea, F., 2012. The sources of energy for crustal melting and the geochemistry of heat-

632 producing elements. Lithos 153, 278–291. doi:10.1016/j.lithos.2012.01.017.

633 Bouhallier, H., Chardon, D., Choukroune, P., 1995. Strain patterns in Archaean dome-

634 and-basin structures: The Dharwar craton (Karnataka, South India). Earth Planet.

635 Sci. Lett. 135, 57 – 75. doi:10.1016/0012-821X(95)00144-2.

636 Brace, W.F., Schulz, C.H., La Mori, P.N., 1969. Isothermal compressibility of kyanite,

637 andalusite, and sillimanite from synthetic aggregates. J. Geophys. Res. 74, 2089–

638 2098. doi:10.1029/JB074i008p02089.

639 Brown, M., 2006. Duality of thermal regimes is the distinctive characteristic of plate

640 tectonics since the Neoproterozoic. Geology 34, 961. doi:10.1130/G22853A.1.

641 Brown, M., Johnson, T., 2018. Secular change in metamorphism and the onset of

642 global plate tectonics. Am. Mineral. 103, 181–196. doi:10.2138/am-2018-6166.

643 Brown, M., Johnson, T., Gardiner, N.J., 2020. Plate Tectonics and the Archean

644 Earth. Annu. Rev. Earth Planet. Sci. 48, 291–320. doi:10.1146/annurev-earth-

645 081619-052705.

646 Burg, J.P., Gerya, T.V., 2005. The role of viscous heating in Barrovian metamorphism

647 of collisional orogens: thermomechanical models and application to the

648 Lepontine Dome in the Central Alps. J. Metamorph. Geol. 23, 75–95.

649 doi:10.1111/j. 1525-1314.2005.00563.x.

650 Burg, J.P., Schmalholz, S.M., 2008. Viscous heating allows thrusting to overcome

651 crustal-scale buckling: Numerical investigation with application to the Himalayan

- 652 syntaxes. *Earth Planet. Sci. Lett.* 274, 189 – 203. doi:10.1016/j.epsl.2008.07.022.
- 653 Burov, E.B., 2011. Rheology and strength of the lithosphere. *Mar. Pet. Geol.* 28,  
654 1402–1443. doi:10.1016/j.marpetgeo.2011.05.008.
- 655 Burov, E.B., Watts, A.B., et al., 2006. The long-term strength of continental lithosphere:  
656 "jelly sandwich" or crème brûlée"? *GSA today* 16, 4.
- 657 Cagnard, F., Barbey, P., Gapais, D., 2011. Transition between "Archaean-type" and  
658 "modern-type" tectonics: Insights from the Finnish Lapland Granulite Belt. *Precam-*  
659 *brian Res* 187, 127 – 142. doi:10.1016/j.precamres.2011.02.007.
- 660 Cagnard, F., Durrieu, N., Gapais, D., Brun, J.P., Ehlers, C., 2006. Crustal thickening  
661 and lateral flow during compression of hot lithospheres, with particular reference to  
662 Precambrian times. *Terra Nova* 18, 72–78. doi:10.1111/j.1365-3121.2009.00873.  
663 x.
- 664 Cagnard, F., Gapais, D., Barbey, P., 2007. Collision tectonics involving juvenile crust:  
665 The example of the southern Finnish Svecofennides. *Precambrian Res* 154, 125 –  
666 141. doi:10.1016/j.precamres.2006.12.011.
- 667 Capitanio, F.A., Nebel, O., Cawood, P.A., Weinberg, R.F., Chowdhury, P., 2019.  
668 Reconciling thermal regimes and tectonics of the early Earth. *Geology* 47, 923–  
669 927. doi:10.1130/G46239.1.
- 670 Cawood, P.A., Hawkesworth, C.J., Dhuime, B., 2012. The continental record and the  
671 generation of continental crust. *Geol. Soc. Am. Bull.* 125, 14–32. doi:10.1130/  
672 b30722.1.
- 673 Cawood, P.A., Hawkesworth, C.J., Pisarevsky, S.A., Dhuime, B., Capitanio, F.A., Nebel,  
674 O., 2018. Geological archive of the onset of plate tectonics. *Philos. Trans. R. Soc.*  
675 *A: Math. Phys. Eng. Sci.* 376, 20170405. doi:10.1098/rsta.2017.0405.
- 676 Chardon, D., Gapais, D., Cagnard, F., 2009. Flow of ultra-hot orogens: A view from the  
677 Precambrian, clues for the Phanerozoic. *Tectonophysics* 477, 105 – 118.  
678 doi:10.1016/j.tecto.2009.03.008.
- 679 Chardon, D., Jayananda, M., Peucat, J.J., 2011. Lateral constrictional flow of hot oro-  
680 genic crust: Insights from the Neoproterozoic of south India, geological and

- 681 geophysical implications for orogenic plateaux. *Geochem. Geophys. Geosyst.* 12,  
682 n/a–n/a. doi:10.1029/2010gc003398.
- 683 Chopra, P.N., Paterson, M.S., 1984. The role of water in the deformation of dunite.  
684 *Journal of Geophysical Research: Solid Earth* 89, 7861–7876. doi:10.1029/  
685 jb089ib09p07861.
- 686 Choukroune, P., Bouhallier, H., Arndt, N., 1995. Soft lithosphere during periods of  
687 Archaean crustal growth or crustal reworking. *Geol. Soc. London Spec. Publ.* 95,  
688 67–86. doi:10.1144/GSL.SP.1995.095.01.05.
- 689 Condie, K.C., Aster, R.C., van Hunen, J., 2016. A great thermal divergence in the  
690 mantle beginning 2.5 Ga: Geochemical constraints from greenstone basalts and  
691 komatiites. *Geosci. Front.* 7, 543–553. doi:http://dx.doi.org/10.1016/j.gsf.  
692 2016.01.006.
- 693  
694 Condie, K.C., Benn, K., 2006. Archean geodynamics: Similar to or different from  
695 modern geodynamics? *Geophysical Monograph-American Geophysical Union* 164,  
696 47–59. doi:10.1029/164GM05.
- 697 Cruden, A.R., Nasser, M.H.B., Pysklywec, R., 2006. Surface topography and inter-  
698 nal strain variation in wide hot orogens from three-dimensional analogue and two-  
699 dimensional numerical vice models. *Geol. Soc. London Spec. Publ.* 253, 79–104.  
700 doi:10.1144/gsl.sp.2006.253.01.04.
- 701 Duclaux, G., Rey, P., Guillot, S., Ménot, R.P., 2007. Orogen-parallel flow during  
702 continental convergence: Numerical experiments and Archean field examples.  
703 *Geology* 35, 715. doi:10.1130/g23540a.1.
- 704 Duprat-Oualid, S., Yamato, P., Pitra, P., 2013. Major role of shear heating in intra-  
705 continental inverted metamorphism: Inference from a thermo-kinematic parametric  
706 study. *Tectonophysics* 608, 812 – 831. doi:10.1016/j.tecto.2013.07.037.
- 707 Duretz, T., Gerya, T.V., 2013a. Slab detachment during continental collision: Influence  
708 of crustal rheology and interaction with lithospheric delamination. *Tectonophysics*  
709 602, 124 – 140. doi:10.1016/j.tecto.2012.12.024.
- 710 Duretz, T., Gerya, T.V., 2013b. Slab detachment during continental collision: Influence

- 711 of crustal rheology and interaction with lithospheric delamination. *Tectonophysics*  
712 602, 124–140. doi:10.1016/j.tecto.2012.12.024.
- 713 Duretz, T., Petri, B., Mohn, G., Schmalholz, S.M., Schenker, F.L., Müntener, O., 2016.  
714 The importance of structural softening for the evolution and architecture of passive  
715 margins. *Sci. Rep.* 6. doi:10.1038/srep38704.
- 716 Duretz, T., Schmalholz, S.M., Podladchikov, Y.Y., Yuen, D.A., 2014. Physics-controlled  
717 thickness of shear zones caused by viscous heating: Implications for crustal shear  
718 localization. *Geophys. Res. Lett.* 41, 4904–4911. doi:10.1002/2014GL060438.
- 719 Faccenda, M., Gerya, T.V., Chakraborty, S., 2008. Styles of post-subduction collisional  
720 orogeny: Influence of convergence velocity, crustal rheology and radiogenic heat  
721 production. *Lithos* 103, 257 – 287. doi:10.1016/j.lithos.2007.09.009.
- 722 Gapais, D., 2018. Tectonics-mineralisation relationships within weak continental  
723 lithospheres: a new structural framework for Precambrian cratons Relations  
724 tectonique- minéralisation dans les lithosphères continentales chaudes,  
725 applications aux cratons précambriens. *Bulletin de la Société Géologique de*  
726 *France* 189, 14. doi:10.1051/bsgf/2018014.
- 727 Gapais, D., Cagnard, F., Gueydan, F., Barbey, P., Ballèvre, M., 2009. Mountain building  
728 and exhumation processes through time: inferences from nature and models. *Terra*  
729 *Nova* 21, 188–194. doi:10.1111/j.1365-3121.2009.00873.x.
- 730 Gapais, D., Jaguin, J., Cagnard, F., Boulvais, P., 2014. Pop-down tectonics, fluid  
731 channelling and ore deposits within ancient hot orogens. *Tectonophysics* 618, 102 –  
732 106. doi:10.1016/j.tecto.2014.01.027.
- 733 Gapais, D., Pelletier, A., Ménot, R.P., Peucat, J.J., 2008. Paleoproterozoic tectonics  
734 in the Terre Adélie Craton (East Antarctica). *Precambrian Res* 162, 531 – 539.  
735 doi:10.1016/j.precamres.2007.10.011.
- 736 Gapais, D., Potrel, A., Machado, N., Hallot, E., 2005. Kinematics of long-lasting  
737 Paleoproterozoic transpression within the Thompson Nickel Belt, Manitoba,  
738 Canada. *Tectonics* 24, TC3002. doi:10.1029/2004TC001700.
- 739 Gerya, T., 2019a. Geodynamics of the early Earth: Quest for the missing paradigm.  
740 *Geology* 47, 1006–1007. doi:10.1130/focus102019.1.

- 741  
742 Gerya, T., 2019b. Introduction to numerical geodynamic modelling. 2nd ed., Cam-  
743 bridge University Press. doi:10.1017/9781316534243.
- 744 Gerya, T.V., Perchuk, L.L., Maresch, W.V., Willner, A.P., 2004. Inherent gravitational  
745 instability of hot continental crust: Implications for doming and diapirism in  
746 granulitefacies terrains, in: Gneiss Domes in Orogeny. Geological Society of  
747 America. doi:10.1130/0-8137-2380-9.97.
- 748 Gerya, T.V., Yuen, D.A., 2003. Rayleigh–Taylor instabilities from hydration and  
749 melting propel ‘cold plumes’ at subduction zones. *Earth Planet. Sci. Lett.* 212,  
750 47–62. doi:10.1016/S0012-821X(03)00265-6.
- 751 Goes, S., Hasterok, D., Schutt, D.L., Klöcking, M., 2020. Continental lithospheric  
752 temperatures: A review. *Phys. Earth Planet. In.* 306, 106509.  
753 doi:10.1016/j.pepi.2020.106509.
- 754 Gray, R., Pysklywec, R.N., 2010. Geodynamic models of Archean continental collision  
755 and the formation of mantle lithosphere keels. *Geophys. Res. Lett.* 37.  
756 doi:10.1029/2010GL043965.
- 757 Hansen, F.D., Carter, N.L., 1983. Semibrittle creep of dry and wet Westerly granite at  
758 1000 MPa, in: The 24th US Symposium on Rock Mechanics (USRMS), American  
759 Rock Mechanics Association, College Station, Texas.
- 760 Hawkesworth, C.J., Brown, M., 2018. Earth dynamics and the development of plate  
761 tectonics. *Philos. Trans. R. Soc. A: Math. Phys. Eng. Sci.* 376, 20180228. doi:10.  
762 1098/rsta.2018.0228.
- 763 Hirth, G., Kohlstedt, D., 2004. Rheology of the Upper Mantle and the Mantle Wedge: A  
764 View from the Experimentalists. American Geophysical Union (AGU). chapter Chap-  
765 ter 6. pp. 83–105. doi:10.1029/138GM06.
- 766 Holder, R.M., Viète, D.R., Brown, M., Johnson, T.E., 2019. Metamorphism and the  
767 evolution of plate tectonics. *Nature* 572, 378–381. doi:10.1038/s41586-019-1462-  
768 2.
- 769 Jackson, J.A., 2002. Strength of the continental lithosphere: time to abandon the jelly

- 770 sandwich? *GSA today* 12, 4–10.
- 771 Jaupart, C., Mareschal, J.C., Larotsky, L., 2016. Radiogenic heat production in the  
772 continental crust. *Lithos* 262, 398–427. doi:10.1016/j.lithos.2016.07.017.
- 773 Johnson, T.E., Kirkland, C.L., Gardiner, N.J., Brown, M., Smithies, R.H., Santosh, M.,  
774 2019. Secular change in TTG compositions: Implications for the evolution of  
775 Archaean geodynamics. *Earth Planet. Sci. Lett.* 505, 65–75. doi:10.1016/j.epsl.  
776 2018.10.022.
- 777 Keller, T., May, D.A., Kaus, B.J.P., 2013. Numerical modelling of magma dynamics  
778 coupled to tectonic deformation of lithosphere and crust. *Geophys. J. Int.* 195, 1406–  
779 1442. doi:10.1093/gji/ggt306.
- 780 Kiss, D., Duretz, T., Schmalholz, S.M., 2020. Tectonic inheritance controls nappe  
781 detachment, transport and stacking in the Helvetic nappe system, Switzerland:  
782 insights from thermomechanical simulations. *Solid Earth* 11, 287–305.  
783 doi:10.5194/se-11-287-2020.
- 784 Kiss, D., Podladchikov, Y., Duretz, T., Schmalholz, S.M., 2019. Spontaneous gener-  
785 ation of ductile shear zones by thermal softening: Localization criterion, 1D to 3D  
786 modelling and application to the lithosphere. *Earth Planet. Sci. Lett.* 519, 284–296.  
787 doi:10.1016/j.epsl.2019.05.026.
- 788 Lenardic, A., 2018. The diversity of tectonic modes and thoughts about transitions  
789 between them. *Philos. Trans. R. Soc. A: Math. Phys. Eng. Sci.* 376, 20170416.  
790 doi:10.1098/rsta.2017.0416.
- 791 Liao, J., Gerya, T., 2017. Partitioning of crustal shortening during continental collision:  
792 2-D thermomechanical modeling. *Journal of Geophysical Research: Solid Earth*  
793 122, 592–606. doi:10.1002/2016JB013398.
- 794 Mareschal, J.C., Jaupart, C., 2013. Radiogenic heat production, thermal regime and  
795 evolution of continental crust. *Tectonophysics* 609, 524–534.  
796 doi:10.1016/j.tecto.2012.12.001.
- 797 Martin, H., Moyen, J.F., 2002. Secular changes in tonalite-trondhjemite-granodiorite  
798 composition as markers of the progressive cooling of Earth. *Geology* 30, 319–322.

- 799 doi:10.1130/0091-7613(2002)030<0319:SCITTG>2.0.CO;2.
- 800 Miyashiro, A., 1961. Evolution of Metamorphic Belts. *J. Petrol.* 2, 277–311. doi:10.  
801 1093/petrology/2.3.277.
- 802
- 803 Nebel, O., Capitanio, F.A., Moyen, J.F., Weinberg, R.F., Clos, F., Nebel-Jacobsen, Y.J.,  
804 Cawood, P.A., 2018. When crust comes of age: on the chemical evolution of  
805 Archaean, felsic continental crust by crustal drip tectonics. *Philos. Trans. R. Soc. A:  
806 Math. Phys. Eng. Sci.* 376, 20180103. doi:10.1098/rsta.2018.0103.
- 807 Palin, R.M., Santosh, M., 2020. Plate tectonics: What, where, why, and when?  
808 *Gondwana Res.* doi:10.1016/j.gr.2020.11.001.
- 809 Palin, R.M., Santosh, M., Cao, W., Li, S.S., Hernández-Urbe, D., Parsons, A., 2020.  
810 Secular change and the onset of plate tectonics on Earth. *Earth Sci. Rev.*  
811 207, 103172. URL: [https://www.sciencedirect.com/science/article/pii/  
812 S001282522030218X](https://www.sciencedirect.com/science/article/pii/S001282522030218X), doi:10.1016/j.earscirev.2020.103172.
- 813 Perchuk, A.L., Safonov, O.G., Smit, C.A., van Reenen, D.D., Zakharov, V.S., Gerya,  
814 T.V., 2018. Precambrian ultra-hot orogenic factory: Making and reworking of conti-  
815 nental crust. *Tectonophysics* 746, 572–586. doi:10.1016/j.tecto.2016.11.041.
- 816 Petri, B., Duretz, T., Mohn, G., Schmalholz, S.M., Karner, G.D., Müntener, O., 2019.  
817 Thinning mechanisms of heterogeneous continental lithosphere. *Earth Planet. Sci.*  
818 *Lett.* 512, 147–162. doi:10.1016/j.epsl.2019.02.007.
- 819 Poh, J., Yamato, P., Duretz, T., Gapais, D., Ledru, P., 2020. Precambrian deformation  
820 zones in compressional tectonic regimes: a numerical perspective. *Tectonophysics*  
821 777, 1–17. doi:10.1016/j.tecto.2020.228350.
- 822 Poli, S., Schmidt, M.W., 2002. Petrology of Subducted Slabs. *Annu. Rev. Earth Planet.*  
823 *Sci.* 30, 207–235. doi:10.1146/annurev.earth.30.091201.140550.
- 824
- 825 Ranalli, G., 1995. *Rheology of the Earth*. Second ed., Springer Science & Business  
826 Media.
- 827 Ranalli, G., 1997. Rheology of the lithosphere in space and time. *Geol. Soc. London*  
828 *Spec. Publ.* 121, 19–37. doi:10.1144/gsl.sp.1997.121.01.02.

- 829 Reuber, G., Kaus, B.J.P., Schmalholz, S.M., White, R.W., 2016. Nonlithostatic pres-  
830 sure during subduction and collision and the formation of (ultra)high-pressure rocks.  
831 *Geology* 44, 343–346. doi:10.1130/G37595.1.
- 832 Rey, P.F., Coltice, N., 2008. Neoproterozoic lithospheric strengthening and the coupling  
833 of Earth's geochemical reservoirs. *Geology* 36, 635–638. doi:10.1130/G25031A.1.
- 834 Rey, P.F., Coltice, N., Flament, N., 2014. Spreading continents kick-started plate  
835 tectonics. *Nature* 513, 405–408. doi:10.1038/nature13728.
- 836 Rey, P.F., Houseman, G., 2006. Lithospheric scale gravitational flow: the impact of  
837 body forces on orogenic processes from Archaean to Phanerozoic. *Geol. Soc. Lon-*  
838 *don Spec. Publ.* 253, 153–167. doi:10.1144/gsl.sp.2006.253.01.08.
- 839 Rogers, J.J.W., Santosh, M., 2004. *Continents and Supercontinents*. Oxford University  
840 Press, New York. doi:10.1093/oso/9780195165890.001.0001.
- 841 Rolandone, F., Jaupart, C., Mareschal, J.C., Gariépy, C., Bienfait, G., Carbonne, C.,  
842 Lapointe, R., 2002. Surface heat flow, crustal temperatures and mantle heat flow in  
843 the Proterozoic Trans-Hudson Orogen, Canadian Shield. *Journal of Geophysical*  
844 *Research: Solid Earth* 107, ETG 7–1–ETG 7–19. doi:10.1029/2001JB000698.
- 845 Schmalholz, S.M., Mancktelow, N.S., 2016. Folding and necking across the scales: a  
846 review of theoretical and experimental results and their applications. *Solid Earth* 7,  
847 1417–1465. doi:10.5194/se-7-1417-2016.
- 848 Schmid, S.M., Kissling, E., Diehl, T., van Hinsbergen, D.J.J., Molli, G., 2017. Ivrea  
849 mantle wedge, arc of the Western Alps, and kinematic evolution of the Alps–  
850 Apennines orogenic system. *Swiss J Geosci* 110, 581–612. doi:10.1007/s00015-  
851 016-0237-0.
- 852 Schmidt, M.W., Poli, S., 1998. Experimentally based water budgets for dehydrating  
853 slabs and consequences for arc magma generation. *Earth Planet. Sci. Lett.* 163,  
854 361 – 379. doi:10.1016/s0012-821x(98)00142-3.
- 855 de Sigoyer, J., Guillot, S., Dick, P., 2004. Exhumation of the ultrahigh-pressure Tso  
856 Morari unit in eastern Ladakh (NW Himalaya): A case study. *Tectonics* 23, 1–18.  
857 doi:10.1029/2002tc001492.

- 858 Sizova, E., Gerya, T., Brown, M., Perchuk, L.L., 2010. Subduction styles in the Pre-  
859 cambrian: Insight from numerical experiments. *Lithos* 116, 209–229.  
860 doi:10.1016/j.lithos.2009.05.028.
- 861 Sizova, E., Gerya, T., Stüwe, K., Brown, M., 2015. Generation of felsic crust in the  
862 Archean: A geodynamic modeling perspective. *Precambrian Res* 271, 198–224.  
863 doi:10.1016/j.precamres.2015.10.005.
- 864 Sokoutis, D., Willingshofer, E., 2011. Decoupling during continental collision and intra-  
865 plate deformation. *Earth Planet. Sci. Lett.* 305, 435–444.  
866 doi:10.1016/j.epsl.2011.03.028.
- 867 Tang, M., Chen, K., Rudnick, R.L., 2016. Archean upper crust transition from mafic to  
868 felsic marks the onset of plate tectonics. *Science* 351, 372–375. doi:10.1126/  
869 science.aad5513.
- 870 Thielmann, M., Kaus, B.J.P., 2012. Shear heating induced lithospheric-scale  
871 localization: Does it result in subduction? *Earth Planet. Sci. Lett.* 359-360, 1 – 13.  
872 doi:10.1016/j.epsl.2012.10.002.
- 873 Turcotte, D., Schubert, G., 2014. *Geodynamics*. Cambridge University Press. doi:10.  
874 1017/CBO9780511843877.
- 875  
876 Vogt, K., Gerya, T.V., 2014. From oceanic plateaus to allochthonous terranes:  
877 Numerical modelling. *Gondwana Res.* 25, 494–508. doi:10.1016/j.gr.2012.11.002.
- 878 Yamato, P., Burov, E., Agard, P., Le Pourhiet, L., Jolivet, L., 2008. HP-UHP exhumation  
879 during slow continental subduction: Self-consistent thermodynamically and thermo-  
880 mechanically coupled model with application to the Western Alps. *Earth Planet. Sci.*  
881 *Lett.* 271, 63 – 74. doi:https://doi.org/10.1016/j.epsl.2008.03.049.
- 882 Yamato, P., Duretz, T., Angiboust, S., 2019. Brittle/Ductile Deformation of Eclogites:  
883 Insights From Numerical Models. *Geochem. Geophys. Geosyst.* 20, 3116–3133.  
884 doi:10.1029/2019GC008249.
- 885 Yamato, P., Mouthereau, F., Burov, E., 2009. Taiwan mountain building: Insights from  
886 2-D thermomechanical modelling of a rheologically stratified lithosphere. *Geophys.*  
887 *J. Int.* 176, 307–326. doi:10.1111/j.1365-246X.2008.03977.x.

## Tables and Figures

Table 1: Rheological and thermal values used in our study. References for rheological flow laws and partial melting are: a = Ranalli (1997); b = Ranalli (1995); c = Hansen and Carter (1983); d = Chopra and Paterson (1984); e = Schmidt and Poli (1998); f = Poli and Schmidt (2002); g = Turcotte and Schubert (2014); h = Gerya (2019b). References for thermal properties are: i = Turcotte and Schubert (2014); j = Brace et al. (1969); k = Bea (2012).

Figure 1: [A] Thermal profiles (in red) and yield strength envelopes (in black) for the two reference models in compression (values used in Table 1). Coloured squares indicate position of reference model in parametric study in Fig. 3 and in subsequent figures. [B] The 2D thermo-mechanical model configuration and boundary conditions (see text for details).  $V$  represents the model's convergence and output velocities which was computed from  $\dot{\epsilon}_{BG}$  to satisfy mass balance.

Figure 2: Distribution of ancient-style and modern-style deformation modes obtained from our 2D parametric study (see Supplementary Data, Fig. S1). The vertical and horizontal axes correspond to  $T_{\text{Moho}}$  and  $\dot{\epsilon}_{BG}$ , respectively. Classifying ancient or modern-style tectonics is determined by the characterisation of deformation of the upper parts of the crust and lithospheric mantle by three main factors (see end of Section 1.2). The selected reference models (from Fig. 1B) to be referred to the rest of the investigation corresponds to the coloured boxes (red: Ancient-style tectonics; blue, modern-style tectonics). The transition from ancient to modern-style tectonics remains qualitative until the 1D parametric studies in Fig. 11A and D.

Figure 3: Composition (top), viscosity (middle) and accumulated strain (bottom) fields for reference models after ca. 320 km of horizontal shortening. [A] Reference model displaying cusping of the sedimentary layer, low topography and by a Moho remaining flat, [B] Reference model for modern-style tectonics display the formation of high viscosity wedges (i.e., Pop-downs), formation of thrusts and shear zones in the upper parts of the crust and lithospheric mantle, and high topography. Isobars are represented by the white and blue solid lines in the composition (top) and viscosity (centre) plots, respectively. Isotherms are represented by the black and white solid lines in the composition (top) and viscosity (middle) plots, respectively. The upper and lower dashed lines shown in the accumulated strain field (down) highlights the extent of the sedimentary layer and Moho, respectively.

Figure 4: Topography evolution up to ca. 320 km of horizontal shortening in the two reference models, [A] Ancient-style tectonics and [B] Modern-style tectonics.

Figure 5: Role of shear heating on deformation in ancient-style tectonics reference model after ca. 320 km of horizontal shortening. The deformation features for both models exhibit similar distributed buckling and cusping of the sedimentary layer. Legends for isotherms, isobars and dashed lines are as for Fig. 3.

Figure 6: Role of shear heating on deformation in modern-style tectonics reference model after ca. 160 km of horizontal shortening. Legends for isotherms, isobars and dashed lines are as for Fig. 3.

Figure 7: Role of crustal rheology using weak crust on the [A] ancient-style and [B] modern-style reference models after ca. 320 km of shortening. In [A], deformation of the crust remains distributed with well-established convecting partially melted at the lower parts of the crust. In [B], deformation becomes symmetrical with the burial of pop-downs and a downward deflection of the Moho. Crustal thickness at the centre reached to approximately 100 km. Legends for isotherms, isobars and dashed lines are as for Fig. 3.

Figure 8: Role of crustal rheology using strong crust on the [A] ancient-style and [B] modern-style reference models after ca. 320 km of shortening. In [A], the sedimentary cusps begin to generate a series of inverse faults while maintaining a flat Moho. In [B], dominant shear localisation is accompanied with the buckling of the lithospheric mantle and thrusts at the crust. Legends for isotherms, isobars and dashed lines are as for Fig. 3.

Figure 9: Role of [A] moderate and [B] low  $H_R$  crustal radiogenic heat production values on the ancient-style reference model after ca. 320 km of horizontal shortening. In both models, deformation patterns are characterised with the cusping of sedimentary layer and maintaining a flat Moho. In [A], deformation patterns remain comparable to the reference model in Fig. 3A. In [B], the number of folds at the upper parts of the crust decreased indicating an increase in lateral distance when compared to [A]. Additionally, the number of high strain accumulation at the Moho in [B] has increased from 1 to 3. Legends for isotherms, isobars and dashed lines are as for Fig. 3.

Figure 10: Role of moderate and low  $H_R$  crustal radiogenic heat production values on the modern-style reference model based on snapshots of the composition (top), viscosity (centre) and accumulated strain (bottom) fields after ca. 320 km and 280 km of horizontal shortening in [A] and [B], respectively. Thrusts of the upper parts of the crust and shearing of the lithospheric mantle dominate both models with reduced  $H_R$ . In [A], two prominent shear zones are located at lithospheric mantle. The lithospheric mantle is observed to bend at the centre while maintaining a lithospheric-scaled shear zone in [B]. Legends for isotherms, isobars and dashed lines are as for Fig. 3.

Figure 11: Results from the 1D parametric study displaying [A] the maximum strength of the crust, [B] the influence of the crustal rheology and [C] the influence of the radiogenic heat production ( $H_R$ ). Red and blue squares correspond to the ancient and modern-style tectonics reference models, respectively (see Fig. 3). The dark circles and diamonds represent identified ancient and modern-style tectonics in the parametric study (seen in Fig. 4 and Supplementary Data, Fig. S1). Solid black line represents the suggested contour maximum crustal strength of ca. 300 MPa as a first order transition from ancient to modern-style tectonics. This contour shifts vertically based on the variations of crustal strength and  $H_R$ . [D] Parametric study varying  $T_{\text{Moho}}$  and  $\dot{\epsilon}_{BG}$  considering the dislocation creep of dry olivine (i.e., lithospheric mantle), applied velocity ( $v$ ), model length ( $L_x$ ) and at 50% horizontal shortening to evaluate the localisation criterion for subduction initiation in Kiss et al. (2019). This criterion is evaluated based on the temperature difference caused by shear heating ( $T_{\text{SH}}$ ) and Moho temperature ( $T_{\text{Moho}}$ ). The parametric study indicates the temperature difference required for modern-style tectonics begins at ca. 225°C. When compared to the maximum crustal strength of ca. 300 MPa, this criterion provides an excellent fit.

## Supplementary Data

Supplementary Data, Figure S1: 2D parametric study of the viscosity and accumulated strain fields after ca. 320 km of shortening. Primary parameters varied are Moho temperature ( $T_{\text{Moho}}$ ) and background strain rate ( $\dot{\epsilon}_{BG}$ ) that defines the geotherm and convergence velocity, respectively (explained in Fig. 1). The rheology and radiogenic heat production applied to the crust of the model is Dry Westerly Granite (Hansen and Carter, 1983) and  $2.0 \mu\text{W}\cdot\text{m}^{-3}$ , respectively. Dashed lines represent the outline of the sedimentary layer and the Moho. The 500 and 800 MPa isobars are represented by blue solid lines in the viscosity (top) plots. Isotherms are represented by solid white lines in increments of  $100^\circ\text{C}$  (from  $100^\circ\text{C}$  to  $700^\circ\text{C}$ ) in the model's viscosity and accumulated strain fields. Arrows shown in the models' viscosity fields are not drawn according to scale. The deformation modes are controlled by the intensity of  $\dot{\epsilon}_{BG}$  which is referred in Fig. 2. Models identified as more ancient-style (in red frames) have distributed deformation and minimal shear zone generation at the upper parts of the crust and lithospheric mantle, low topography ranges and homogeneous  $P$ - $T$  distributions. In contrast, models identified as more modern-style (in blue frame) have dominant thrusts and shear zones at the crust and lithospheric mantle, high topography ranges and asymmetric distribution of  $P$ - $T$  lines.



**Research Highlights**

- The magnitude of the crustal shear stress dictates the tectonic style.
- Modern style tectonics occurs for a maximum crustal shear stress  $> 300$  MPa.
- Shear heating is a key factor for strain localisation in modern style tectonics.

**CRediT author statement for Gondwana Research Submission**

**Jonathan Poh:** Conceptualisation, Methodology, Investigation, Writing – Original Draft, Writing – Review & Editing.

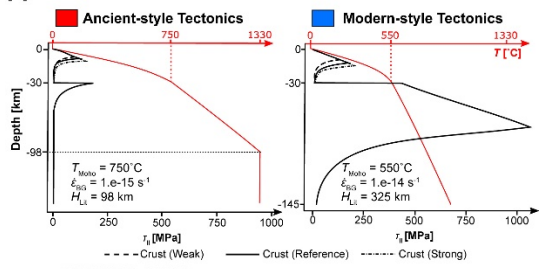
**Philippe Yamato:** Supervision, Software, Resources, Writing – Review & Editing, Conceptualisation, Validation, Data Curation, Visualisation

**Thibault Duret:** Software, Validation, Methodology, Writing – Review & Editing, Investigation, Data Curation, Visualisation

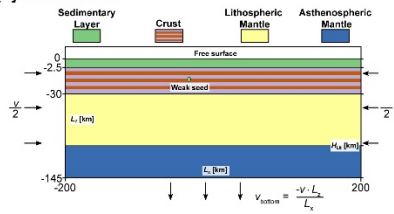
**Denis Gapais:** Conceptualisation, Validation.

**Patrick Ledru:** Validation, Funding acquisition, Writing – Review & Editing

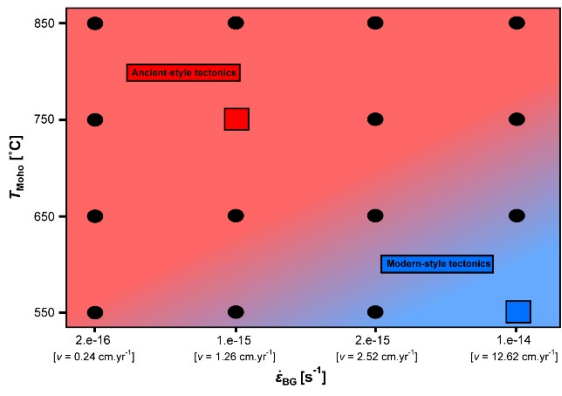
[A] REFERENCE MODELS YIELD STRENGTH ENVELOPES

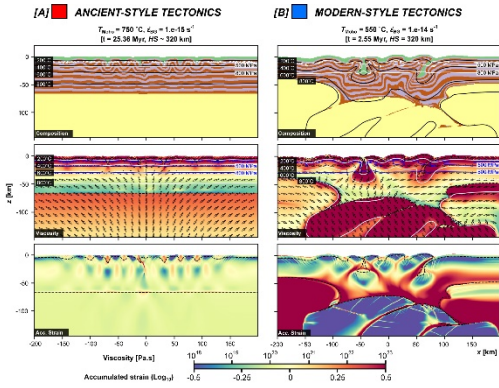


[B] MODEL SETUP



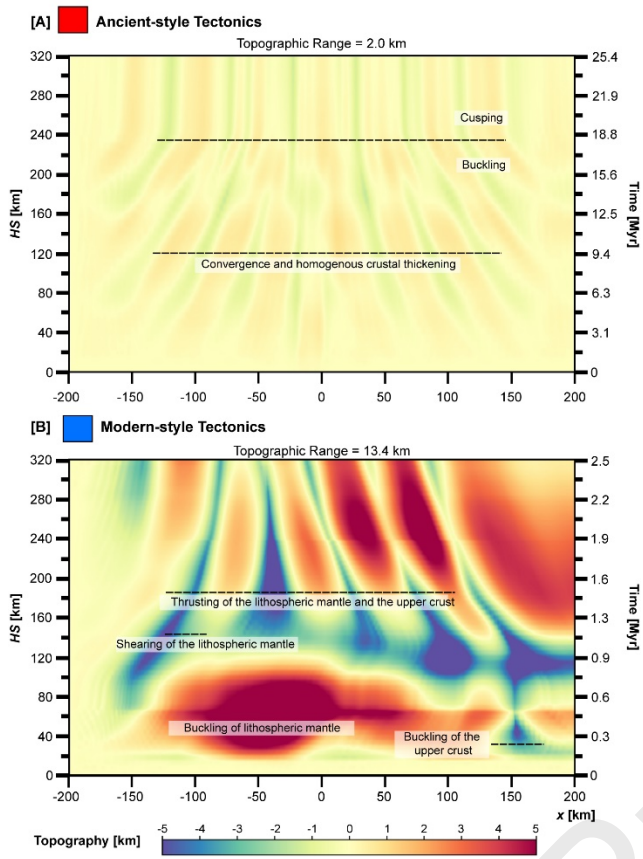
Journal Pre-proofs

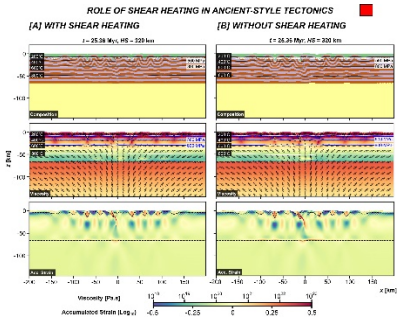


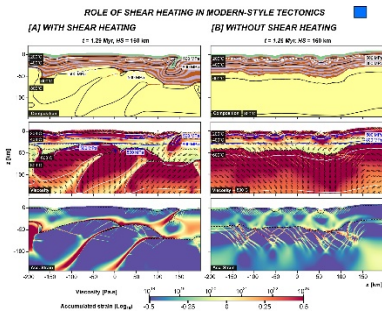


Journal Pre-proofs

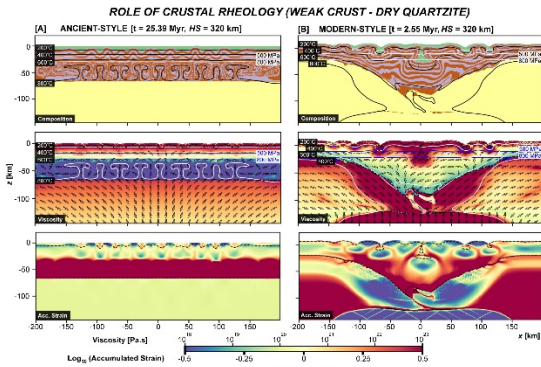
## REFERENCE MODELS' TOPOGRAPHY EVOLUTION



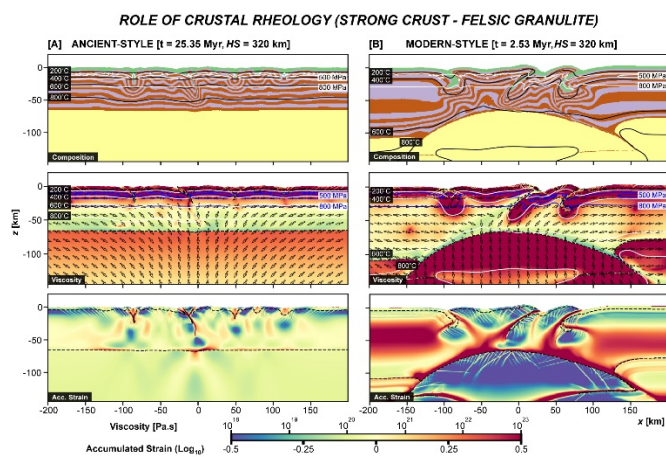


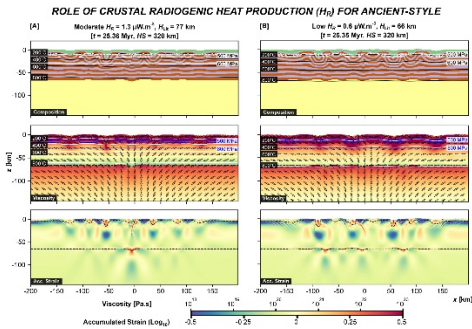


Journal Pre-proofs

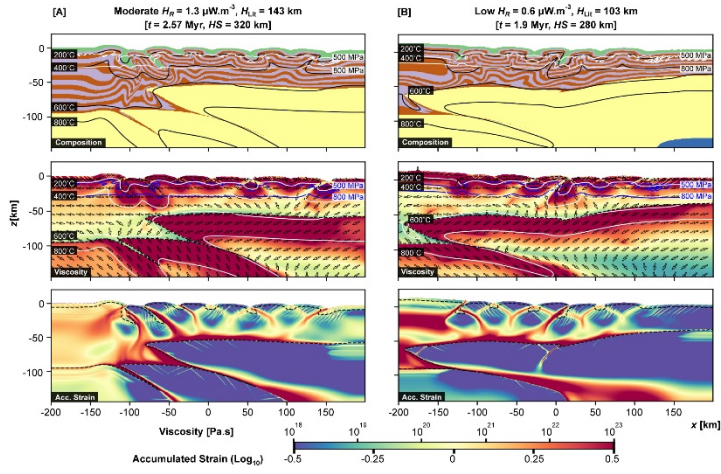


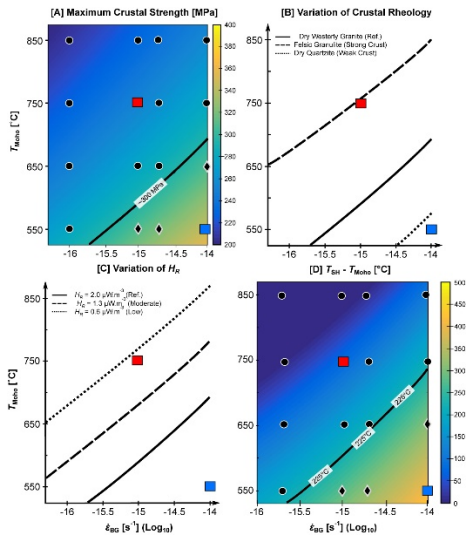
Journal Pre-proofs





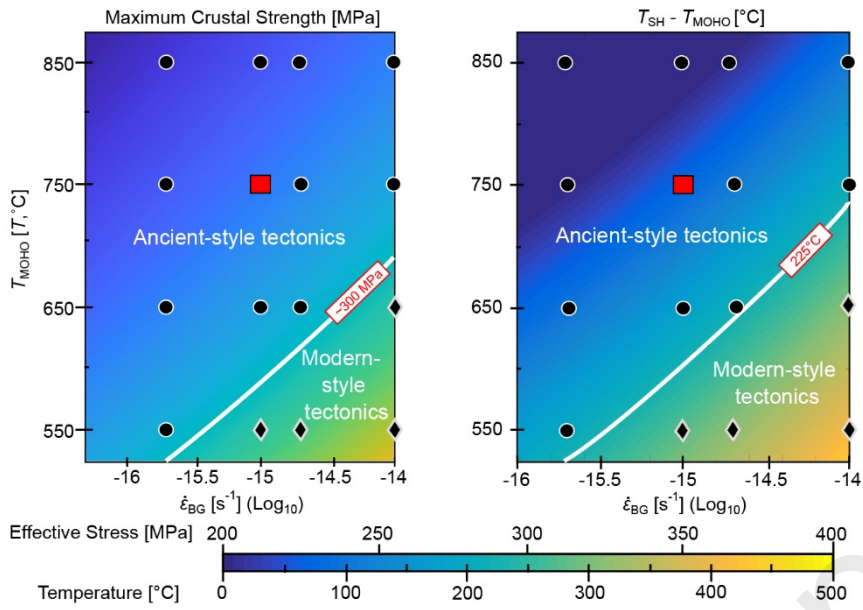
Journal Pre-proofs

ROLE OF CRUSTAL RADIOGENIC HEAT PRODUCTION ( $H_R$ ) FOR MODERN-STYLE



Journal Pre-proofs

Proxies that predict tectonic style:



**Research Highlights**

- The magnitude of the crustal shear stress dictates the tectonic style.
- Modern style tectonics occurs for a maximum crustal shear stress  $> 300$  MPa.
- Shear heating is a key factor for strain localisation in modern style tectonics.

**CRedit author statement for Gondwana Research Submission**

**Jonathan Poh:** Conceptualisation, Methodology, Investigation, Writing – Original Draft, Writing – Review & Editing.

**Philippe Yamato:** Supervision, Software, Resources, Writing – Review & Editing, Conceptualisation, Validation, Data Curation, Visualisation

**Thibault Duret:** Software, Validation, Methodology, Writing – Review & Editing, Investigation, Data Curation, Visualisation

**Denis Gapais:** Conceptualisation, Validation.

**Patrick Ledru:** Validation, Funding acquisition, Writing – Review & Editing

Each named author has substantially contributed to conducting the underlying research and drafting this manuscript. Additionally, to the best of our knowledge, the named authors have no conflict of interest, financial or otherwise.

Yours sincerely,  
Dr. Jonathan Poh and co-authors

**Corresponding Author**

Dr. Jonathan Poh  
Energy Research Institute @ NTU,  
Nanyang Technological University,  
CleanTech One, 1 Cleantech Loop, #06-04,  
637141, Singapore  
jonathanpoh87@gmail.com

**Additional Contact**

Professor Philippe Yamato  
Géosciences Rennes (UMR CNRS 6118)  
University of Rennes 1 – Campus Beaulieu  
CS 74205, F-35042 Rennes Cedex France  
philippe.yamato@univ-rennes1.fr